Electronic Supplementary Material (ESI) for Nanoscale.

Electronic Supplementary Information: Substrate adhesion evolves non-monotonically with processing time in millimeter-scale aligned carbon nanotube arrays

Ashley L. Kaiser,*[a] **Dale L. Lidston,**[b] **Sophie C. Peterson,**[c] **Luiz H. Acauan,**[b] **Stephen A. Steiner III,**[b] **Roberto Guzman de Villoria,**[b,d] **Amy R. Vanderhout,**[b] **Itai Y. Stein,***[b,e] **and Brian L. Wardle***[b]

[a] *Department of Materials Science and Engineering, Massachusetts Institute of Technology, 77 Massachusetts Ave, Cambridge, MA 02139, USA. Email: alkaiser@alum.mit.edu*
[b] *Department of Aeronautics and Astronautics, Massachusetts Institute of Technology, 77 Massachusetts Ave, Cambridge, MA 02139, USA. E-mail: iys@alum.mit.edu; wardle@mit.edu*
[c] *Department of Mechanical Engineering, Massachusetts Institute of Technology, 77 Massachusetts Ave, Cambridge, MA 02139, USA*
[d] *Current Affiliation: Department of Mechanical Engineering, University of Salamanca, Campus Viriato, Avenida Requejo, 33, 49022 Zamora, Spain*
[e] *Current Affiliation: Cross-cutting Urgent Innovation Cell, The MITRE Corporation, Bedford, MA 01730, USA. The author's affiliation with the MITRE Corporation is provided for identification purposes only, and is not intended to convey or imply MITRE's concurrence with, or support for, the positions, opinions or viewpoints expressed by the author. Approved for Public Release; Distribution Unlimited. Public Release Case Number 20-1511*

S1 Carbon Nanotube-Substrate Adhesion Modeling

The following presents the derivation of the fiber-substrate adhesion model, here applied to aligned carbon nanotube (CNT) arrays, and the model parameters and system geometry shown in Fig. S1 are reproduced from Fig. 2 in the main text for illustrative purposes. We take the aligned CNT array as composed of n vertical, non-interacting, and hollow multiwall CNTs with a cylindrical column structure and uniform inter-CNT spacing Γ. Only the annular CNT bases contact the growth substrate, which is comprised of Fe catalyst particles on $Al_2O_3/SiO_2/Si$ layers (Si wafer), and the CNTs are synthesized *via* catalytic base growth chemical vapor deposition (CVD; see Methods in the main text). As shown in Fig. S1, the CNT-substrate contact area is experimentally determined to be between the annular CNT base and the CVD growth-induced carbon layer covering the Fe catalyst, which follows a hollow cylinder geometry[1,2] with one-dimensional thickness equal to the total CNT wall thickness, a (*i.e.* outer radius, R_o – fixed inner radius, R_i). Here, a is assumed to be an average for the entire CNT array, R_i is constant with CNT process time (t_p), and the variable length R_o (and therefore a) increases with t_p. The CNT array follows two Modes as a function of t_p, as discussed in the main text: Mode I steady CNT array growth for t_p = 9 to ∼40 min, and Mode II post-growth carbon deposition for t_p ∼40 to 80 min, following abrupt vertical growth termination at 40 min.

The CNT-substrate interaction is assumed to occur *via* the dispersive adhesion attraction mechanism based on the intermolecular forces acting between the molecules of both contacting materials.[3,4] Therefore, the maximum tensile pull-off stress required to separate the cm-scale CNT array from its substrate (σ_{a-s}) is derived based on the Johnson-Kendall-Roberts (JKR) contact mechanics theory for relatively compliant, elastic solids that balances elastic and surface energy,[3–5] where new surfaces are created after CNT array pull-off. The CNT array, which has an effective elastic axial continuum modulus (E) that implicity captures CNT-CNT interactions[6–8] and waviness effects,[9,10] is modeled as a group of annular contacts (n CNTs)

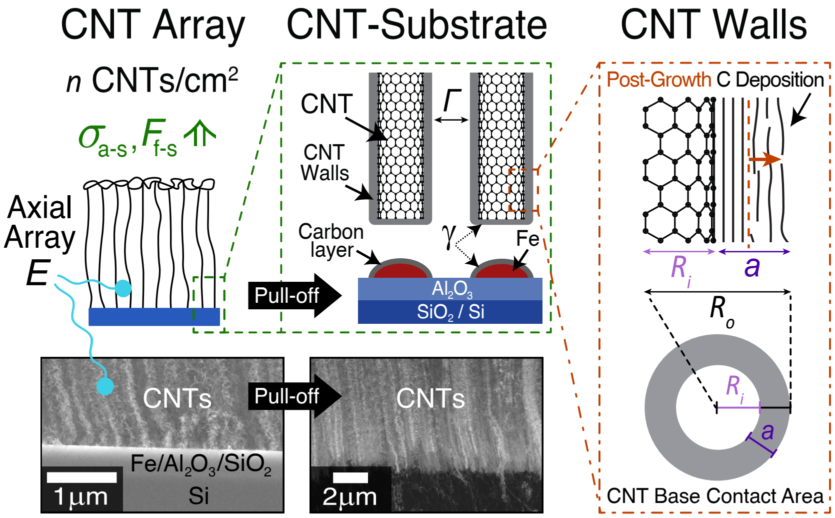

Fig. S1 Overview of the nanofiber array system geometry used to model CNT-substrate adhesion *via* hollow cylinder geometry. Illustrations showing that the maximum pull-off force (F_{a-s}) and therefore σ_{a-s} and F_{f-s} are obtained by separating an aligned CNT array from its carbon-covered catalyst layer/substrate (carbon cap/$Fe/Al_2O_3/SiO_2/Si$), as shown by two SEM images demonstrating CNT array-substrate separation. Additional carbon, which deposits on the outer CNT walls to increase a and F_{a-s} during Mode II ('Post-Growth') is also shown, as well as the inner CNT radius (R_i), outer CNT radius (R_o), total number of CNTs contributing to F_{a-s} (number density n), inter-CNT spacing (Γ), effective CNT array elastic axial modulus (E), and interfacial CNT-substrate work of adhesion between the two separating layers (γ).

with work of adhesion (γ) between the CNT base and the substrate. $\sigma_{\mathrm{a-s}}$ is determined by the complete detachment of all CNT bases from the substrate *via* the minimization of elastic and surface energy, with no energy dissipation outside the region where separation occurs,[5,11–13] and each CNT has its own adhesion force ($F_{\mathrm{f-s}}$). The substrate is assumed to be orders of magnitude stiffer than the array so that the reduced modulus[5] is approximated as the array modulus E. If this were not the case, *i.e.* if E were in the ∼GPa range, modeling the substrate adhesion of this stiffer array would require additional consideration of energy dissipation outside of the NF-substrate debonding region during pull-off testing,[5,11–13] resulting in more complex analytical relations. Finally, shear/lateral adhesive force contributions from CNT sections lying parallel to the substrate are neglected, which is reasonable due to the vertical CNT growth and negligible CNT compression during the preload prior to the tensile testing performed to measure $\sigma_{\mathrm{a-s}}$.[14]

Therefore, $\sigma_{\mathrm{a-s}}$ can be described both experimentally and *via* the following theoretical framework, which is adapted from the previously-derived substrate adhesion strength of elastic cylinders.[1,5,11] Here, $\sigma_{\mathrm{a-s}}$ is obtained by dividing the maximum measured tensile pull-off force for the bulk array ($F_{\mathrm{a-s}}$) by the apparent CNT array area[12,15] ($A_{\mathrm{array}} \sim 1\ \mathrm{cm}^2$), treating the array as being separated at the maximum stress measured during pull-off:

$$\sigma_{\mathrm{a-s}} = \frac{F_{\mathrm{a-s}}}{A_{\mathrm{array}}} \tag{S1}$$

$\sigma_{\mathrm{a-s}}$ is then divided by n to obtain $F_{\mathrm{f-s}}$, where n [CNTs/cm^2] represents the number density of CNTs contacting the substrate. Similarly, $F_{\mathrm{f-s}}$ can be calculated theoretically and then scaled by n, incorporating the effective CNT array characteristics, to calculate the bulk array adhesion strength $\sigma_{\mathrm{a-s}}$. This is done by first considering the area of each annular surface involved in separating a single CNT/fiber base from the substrate (A_{f}, eqn S2 for an exemplary fiber) as well as the effective CNT/fiber radius (a_{eff}, eqn S3) following hollow cylinder geometry.[1,2]

$$A_{\mathrm{f}} = \pi(R_{\mathrm{o}}^2 - R_{\mathrm{i}}^2) \tag{S2}$$

$$a_{\mathrm{eff}} = \sqrt{\frac{A_{\mathrm{f}}}{\pi}} = (R_{\mathrm{o}}^2 - R_{\mathrm{i}}^2)^{1/2} \tag{S3}$$

Then, the elastic and surface energies present for a single CNT-substrate separation (of a hollow CNT cylinder) creating two new surfaces are calculated (U_{e}, eqn S4, and U_{s}, eqn S5, respectively) to obtain the critical stress at the CNT base responsible for full separation ($\sigma_{\mathrm{critical}}$, eqn S6), *i.e.*, when the surface energy gained equals the elastic energy released, and the total change in energy per unit length ($\delta U_{\mathrm{T}} = \delta U_{\mathrm{e}} + \delta U_{\mathrm{s}}$) with respect to CNT radius is zero.[3–5] This relation incorporates the prefactor $\beta \sim 0.4$ previously used to account for variations in the contact region,[2,5,11] such as geometric irregularities, defects, and surface roughness that can reduce the true contact area in fibrillar systems.[14,16] $F_{\mathrm{f-s}}$ can then be calculated *via* eqn S7.

$$U_{\mathrm{e}} = \frac{1}{2}\frac{-\sigma^2(2A_{\mathrm{f}})}{E} = \frac{-\sigma^2\pi(R_{\mathrm{o}}^2 - R_{\mathrm{i}}^2)}{E} \tag{S4}$$

$$U_{\mathrm{s}} = 4\gamma a_{\mathrm{eff}} = 4\gamma(R_{\mathrm{o}}^2 - R_{\mathrm{i}}^2)^{1/2} \tag{S5}$$

$$\delta U_\mathrm{e} + \delta U_\mathrm{s} = 0 \hookrightarrow \sigma_\mathrm{critical} = \beta\sqrt{\frac{2\gamma E}{\pi(R_\mathrm{o}^2 - R_\mathrm{i}^2)^{1/2}}} \tag{S6}$$

$$F_\mathrm{f-s} = \sigma_\mathrm{critical} A_\mathrm{f} \tag{S7}$$

Here, we consider bulk CNT-substrate adhesion strength that incorporates the full CNT number density, n (*i.e.* all CNTs are separated from the substrate), and therefore $F_\mathrm{f-s}$ for each t_p is calculated *via* eqn S8[15,17] (eqn 2 in the main text), where synchronous CNT separation is assumed for simplicity.[5,12,15] The full relation for $\sigma_\mathrm{a-s}$ is presented in eqn S9, which is reproduced as eqn 1 and plotted along with $F_\mathrm{f-s}$ in Fig. 2 and Fig. 4 in the main text.

$$F_\mathrm{f-s} = \frac{\sigma_\mathrm{a-s}}{n} \tag{S8}$$

$$\hookrightarrow \sigma_\mathrm{a-s} = n\beta\sqrt{8\pi\gamma E(R_\mathrm{o}^2 - R_\mathrm{i}^2)^{3/2}} \tag{S9}$$

Therefore, with inputs of experimental values of $\sigma_\mathrm{a-s}$, R_o, R_i, and E (measured from the initial slope of the stress-strain curves in tensile testing), and inputs of estimated values of β and n (see discussion of n evolution below and in Fig. S2), eqn S9 is used to calculated the expected γ for CNT-substrate adhesion to provide insight into the separating interfaces for this system. Additional details concerning γ, n, and E evolution with t_p for this model are described below, and all experimentally measured and calculated parameter values are shown in Table S1.

Table S1 Experimentally-determined CNT array height (h), CNT array-substrate adhesion strength ($\sigma_\mathrm{a-s}$, *via* eqn S1), CNT wall thickness (a), and CNT array effective elastic axial modulus (E) as a function of process time (t_p), in addition to the calculated CNT number density (n, *via* eqn S10 and Refs. 18 and 19), substrate adhesion force per CNT ($F_\mathrm{f-s}$, *via* eqn S8 using the experimental $\sigma_\mathrm{a-s}$ values), and work of adhesion (γ, *via* eqn S9 using R_i = 3 nm and the corresponding experimental parameters for each t_p), including standard error.

	Measured					**Calculated**		
	t_p [min]	h [mm]	$\sigma_\mathrm{a-s}$ [kPa]	a [nm]	E [MPa]	n [$\times 10^{10}$ cm^{-2}]	$F_\mathrm{f-s}$ [nN]	γ J m^{-2}
Mode I	9	0.88±0.020	40.0±2.5	1.50±0.30	7.35±2.5	2.10±0.21[19]	0.190±0.011	0.032±0.03
	20	2.40±0.060	30.0±3.0	1.40±0.10	10.1±0.99	1.44±0.14	0.208±0.021	0.032±0.01
	30	3.10±0.10	12.5±5.0	2.21±0.20	2.36±0.87	0.587±0.060	0.213±0.085	0.060±0.1
	40	4.40±0.20	15.0±5.0	3.25±0.20	4.72±0.54	0.231±0.023[18]	0.650±0.22	0.14±0.1
Mode II	50	4.70±0.50	145±5.0	3.84±0.21	20.1±3.5	0.231±0.023	6.28±0.22	1.9±0.4
	60	4.60±0.30	270±89	4.55±0.30	88.1±21	0.231±0.023	11.7±3.8	1.2±0.4
	80	4.50±0.30	285±72	6.90±0.30	33.2±15	0.231±0.023	12.3±2.9	1.4±0.7

The average work of adhesion γ, calculated *via* eqn S9 to be 0.066±0.02 J/m^2 in Mode I and 1.5±0.2 J/m^2 in Mode II, is assumed to be constant with t_p in each Mode and signifies twice the surface free energy of the contacting surfaces in Kendall's framework.[4,20] This represents the van der Waals (VDW)-dominated surface interaction energy between the two separating interfaces,[20,21] here the CNT base and the carbon layer surrounding the Fe catalyst (see Figs. S3 − S5). γ is larger in Mode II to account for deposited carbon on CNTs that increases the surface energy compared to the more atomically smooth, graphite-like surfaces in Mode I involved in the separation of the crystalline CNT from the carbon on the catalyst.[13,20] This carbon layer may form during the cooling process due to carbon precipitation from the iron catalyst,[22–24] and it may also become thicker after growth termination due to catalyst deactivation[25–27] and encapsulation by additional carbon during Mode II. The rapid transition to this state at growth termination may account for the discontinuous evolution in CNT-substrate adhesion between the two Modes, as discussed in the main text.

Additionally, no CNTs of height h are observed to remain on the Si wafer surface, which we take to effectively mean that all n CNTs of mm-scale height h that contact both the substrate and the upper silver epoxy layer during tensile testing are removed during CNT array-substrate separation. The measured $\sigma_{\mathrm{a-s}}$ is therefore the product of $F_{\mathrm{f-s}}$ and n, and the evolution of n with t_p is shown in Fig. S2. This is consistent with previous work scaling bulk adhesive properties by the number of contacts,[17] such as for gecko-inspired microfibrillar dry adhesives,[1,5] and recently for micron-tall vertically aligned CNT arrays.[12,15]

The evolution of n with t_p in Fig. S2 was estimated as follows for use in eqns S8 and S9. n at t_p = 9 min was estimated as 2.10×10^{10} CNTs/cm^2 at t_p based on previous measurements of our CNT arrays.[19,28] During Mode I for $t_\mathrm{p} > 9$ min, n is then set to follow a cubic decay to reach $\sim$11% of its original value at growth termination, as this is consistent with previously reported measurements of n decay to $\sim$11% of the original n at termination due to CNT-substrate debonding during growth and the subsequent loss of a self-supporting array structure.[18,29] Incorporating this scaling in eqn S9 is consistent with the experimental Mode I values of E in the expected range of $1-10$ MPa (see Fig. 3 in the main text) based on prior work for similarly CVD-grown aligned CNT arrays[9,10,30] and is consistent with previous observations of n decreasing with t_p towards termination.[18] The Mode I n evolution with t_p is therefore approximated by a cubic fit *via* eqn S10.

$$n(t_\mathrm{p}) = 1.19\times10^{6}(t_\mathrm{p})^3 - 8.23\times10^{7}(t_\mathrm{p})^2 + 9.99\times10^{8}(t_\mathrm{p}) + 1.78\times10^{10} \tag{S10}$$

Continuity in $\sigma_{\mathrm{a-s}}$, $F_{\mathrm{f-s}}$, E, and γ between Mode I and Mode II is not enforced at t_p = 40 min and 50 min (see Fig. 4 in the main text), since more data supplemented by CNT-substrate adhesion simulations are required to accurately characterize the overall scaling of this transition due to complexities in the CVD growth process. Then, in the Post-Growth regime, the lower n value at growth termination (here calculated as 2.31×10^{9} CNTs/cm^2 at t_p = 40 min) is kept constant throughout Mode II (see Fig. S2), as CNT growth in the vertical direction has stopped, and negligible CNT lift-off from the substrate during processing is expected in Mode II. In reality, possible n variation may be attributed to stress build-up at the CNT base with enhanced carbon deposition that may prematurely release CNTs from the substrate, catalyst diffusion and coarsening (which may also be affected by carbon build-up around the catalyst), or additional growth attempts by small-diameter CNTs that would increase n.[18,29] However, these CNTs would be much shorter than the average h for a given t_p (see Fig. S4), and they are not expected to significantly alter $\sigma_{\mathrm{a-s}}$ during CNT-substrate separation, as noted by others.[15] Further simulation studies and *in situ* experimental measurements would be required to corroborate these results by quantifying n evolution at long t_p values extending beyond CNT growth termination. This type of characterization for bulk nanofiber arrays is often quite challenging.

Additionally, while this study considers the averaged, bulk CNT array adhesion strength with effective array properties, it is noted that self-similar individual CNT-to-CNT array scaling behavior likely exists

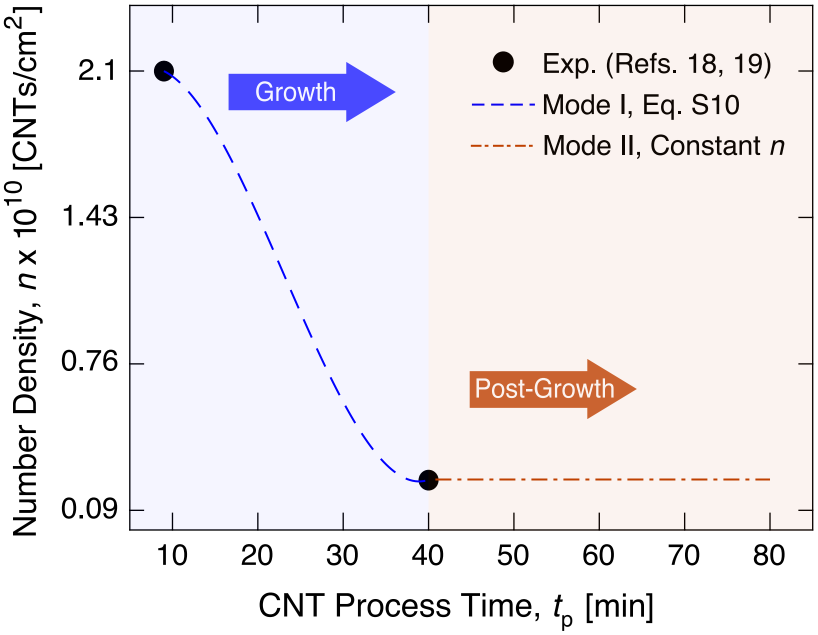

Fig. S2 Plot illustrating the CNT number density (n) evolution with process time (t_p), representing the number of CNTs in contact with the substrate (*i.e.* contributing to F_{a-s}) during the two growth modes. The initial n at t_p = 9 min is calculated to be $\sim$2.1 × 10^{10} CNTs/cm^2 based on the known $\sim$1% CNT volume fraction for a $\sim$1 mm-tall CNT array, which corresponds to an inter-CNT spacing (Γ) of $\sim$70 nm.[19,28] Once growth termination is reached at $t_p \sim 40$ min (onset of Mode II, 'Post-Growth'), n has decayed to $\sim$11% of its original value due to CNT lift-off from the substrate during processing, quantified here *via* a cubic fit.[18,29] This value is set to remain constant as t_p increases further in Mode II, as n decay is assumed to cease because CNT growth in the vertical direction has stopped.

between F_{f-s} and F_{a-s}. More complex models are needed if asynchronous CNT-substrate separation is to be considered, as this behavior has been noted to occur for simulated nanofiber arrays in previous work,[15] and may be suggested by the form of many of the curves in Fig. 3b in the main text. For example, if the higher individual CNT elastic modulus ($E \sim 1$ TPa)[31] is used in eqn S6 leading to eqn S9 for σ_{a-s}, instead of the orders-of-magnitude lower effective array modulus ($E \sim 1-100$ MPa), the correspondingly higher F_{f-s} values would need to be scaled by much smaller n to obtain the same experimental F_{a-s} values, thereby accounting for asynchronous CNT-substrate separation. However, due to this orders-of-magnitude higher E, the individual CNT adhesion mechanics would likely be outside of the JKR regime due to non-local energy dissipation effects not considered in the more compliant bulk fiber array adhesion strength studied here.[5,20] Therefore, more data and multi-scale simulations are required to quantify this phenomenon beyond the bulk array adhesion presented here, which is an avenue for future work.

Finally, increases in E are proportional to the increasing F_{a-s} and a with t_p, which can cause reductions in shear, bending, and torsional contributions to deformation.[9,19] While these CNTs are assumed to be straight and non-interacting, CNT arrays grown by CVD often contain wavy and intertwined individual CNTs. Here, it is assumed that E represents the effective elastic CNT array mechanics, and that the CNTs are effectively straight near the vicinity of their attachment to the catalyst, where their translation in the x-y plane during tensile pull-off is likely sufficiently small and can be neglected.[9,12,19] In the future, additional work to quantify the impact of these morphology-based effects on CNT-substrate adhesion strength will aid in improving adhesion models for stochastic nanofiber arrays and related material systems.

S2 Carbon Nanotube-Substrate Adhesion Testing and Post-Separation Interfacial Characterization

While nanofiber array-substrate adhesion testing in recent years has commonly been done *via* tape peeling (and related shear tests) and nanoscratching, these techniques are not well-suited to the CNT array morphology, since these tests are often only qualitative, may require carefully controlled peel angles, generate large friction forces, and it is often unknown if all CNTs make contact with the tape.[14,30,32,33] Therefore, direct tensile testing-based methods using various 'glues' on the top of an aligned array (allowing for vertical CNT pull-off, see Fig. S3) are often more appropriate for measuring substrate adhesion forces of aligned arrays,[12,15,30,34] and this is applied in this work following the procedure originally reported in Ref. 34.

Therefore, to measure the normal (*i.e.* not shear) aligned CNT array-substrate adhesion strength ($\sigma_{\mathrm{a-s}}$, array failure stress) *via* vertical CNT array pull-off from the Si wafer growth substrate, aluminum scanning electron microscopy (SEM) stubs coated with epoxy were used to mount the CNT-substrate samples in the grips of a Zwick Roell mechanical tester operating in the tensile testing configuration, following Ref. 34 (see Fig. S3). MG Chemicals two-part silver conductive epoxy, selected for its high viscosity and microparticle Ag particles that impede resin infusion into the CNT arrays, was mixed in a 1:1 ratio, and a $\sim$1 mm-thick uniform layer was applied by hand to the flat circular face of an SEM stub using a wooden applicator stick. A CNT array/Si wafer sample (1 cm^2) was positioned on top of the silver epoxy by hand (with the wafer side contacting the epoxy) and cured for at least 4 h at room temperature. Following curing, the SEM stub was inserted into the lower grip of the mechanical tester. Then, a $\sim$1 mm-thick uniform layer of silver epoxy was applied to the flat circular face of a second SEM stub, which was inserted into the upper grip and lowered until it made contact with the top of the CNT array and experienced a small compressive load of $\sim$0.1 N so as not to buckle the array.[12] The load returned to zero as the epoxy relaxed for $\sim$1 min in the SEM stub-CNT interface, and the upper grip was again lowered until $\sim$0.1 N was applied. This process was repeated until the epoxy began to bulge around the edges, after which it was left to cure for at least 4 h at room temperature while mounted in the mechanical tester (see the final assembly illustrated in Fig. S3). In this way, the epoxy bonded the top of the CNT array to the tensile testing grip, where the epoxy's high viscosity was necessary to prevent it from undesirably wicking through the CNT array to the substrate surface (only penetrating by $<$ 30 microns). $\sim$4$-$5 samples for each CNT process time (t_{p} ranging from 9 to 80 min) were tested following ASTM D5179-02 (crosshead speed of 5 cm/min, 500 N load cell), and the load [N] and displacement [mm] were recorded until the Si wafer/CNT array interfaces were ultimately separated. Then, $\sigma_{\mathrm{a-s}}$ was calculated by dividing the maximum tensile load required to separate the entire CNT array from the substrate (*i.e.* $F_{\mathrm{a-s}}$, the maximum force on the load-displacement curves) by the apparent area of the CNT array, $A_{\mathrm{array}} \sim 1$ cm^2, as described in Fig. 3 in the main text.

As shown in Fig. S3, after the aligned CNT arrays were pulled off of the substrate to measure $\sigma_{\mathrm{a-s}}$, the separated CNT-substrate interfaces were characterized *via* SEM. The CNT interface (*i.e.* the CNT roots, or the CNT array base) was additionally characterized by transmission electron microscopy (TEM) and Raman spectroscopy. TEM samples were prepared from the full CNT array length to observe the number of CNT walls, inner diameter, outer diameter, CNT wall thickness, and qualitative carbon character (*i.e.* disordered outer CNT walls). Raman spectroscopy was performed on the bottom of the array to assess the structural quality of the CNT arrays at their growth points. The separated Si wafers and CNT arrays were imaged using SEM with energy-dispersive X-ray spectroscopy (EDS) for in-depth qualitative morphological characterization, including CNT packing, waviness, and wall thickness of the CNTs when viewing the side of the array, morphology and chemical species of the CNT roots, and the morphology of the Si wafer surface including catalyst presence and carbon deposition. SEM was performed using a Zeiss Merlin High-resolution SEM with an accelerating voltage of 5 kV and a 5 mm working distance, with 15 kV and a 10 mm working distance used for EDS. The SEM images in Fig. S4 and Fig. S5 (partially reproduced from

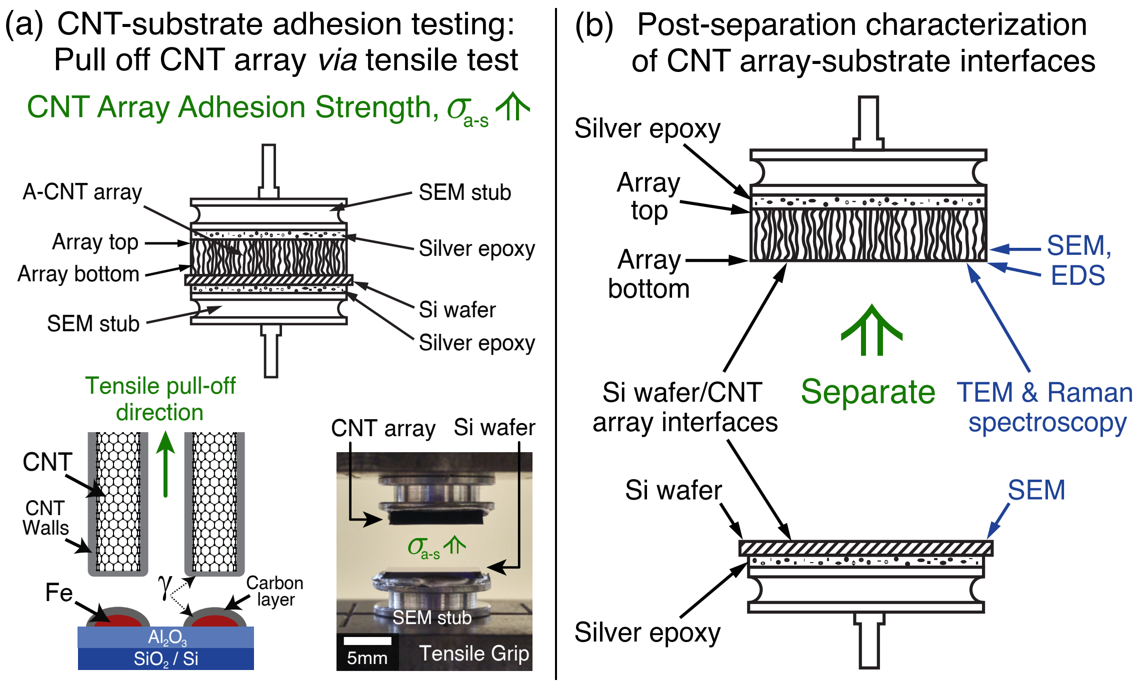

Fig. S3 Overview of the tensile testing setup for an aligned CNT (A-CNT) array to determine its adhesion strength to the substrate ($\sigma_{\mathrm{a-s}}$) and post-testing characterization of the CNT array-substrate interfaces, as adapted from Ref. 34. (a) Illustrations and optical images showing the measurement of $F_{\mathrm{a-s}}$ in a tensile tester *via* vertical CNT array-substrate separation at the CNT-carbon cap-Fe catalyst interface with work of adhesion γ between the separating carbon layers. (b) Illustration showing the imaging and sampling locations of the separated CNT array-substrate interfaces for CNT characterization *via* Raman spectroscopy, scanning electron microscopy (SEM), and transmission electron microscopy (TEM).

Fig. 3 in the main text) show the morphology of the Si wafer surface and CNT roots, respectively, after CNT-substrate separation.

After CNT array-substrate separation, the absence of catalyst pits[15,35] on the wafer surface and the open-ended, iron-free CNT roots on the bottom of the separated array suggest that the Fe catalyst particles remain on the substrate after CNT array pull-off, and the carbon layer remains on top of the Fe catalyst/Si wafer surface as t_{p} increases. This shows that the breaking interface during CNT-substrate separation is between the CNT base and the carbon layer covering the Fe catalyst, as discussed in the main text. Iron is found on the substrates after CNT growth for two main reasons (part of an ongoing study to be published). This is due to the iron catalyst particles that nucleated CNTs and then remained on the substrate after CNT array pull-off, (also noted by the absence of catalyst pits on the wafer and the absence of iron in CNT roots), as well as the iron particles that did not nucleate CNTs, which instead become covered with a carbon layer and are deactivated as a catalyst, thus also remaining on the substrate.

As growth termination is reached at $t_{\mathrm{p}} \sim 40$ mins, extra carbon begins to accumulate at this interface, since carbon precursor gas flows in the reactor while vertical CNT array growth has stopped. After growth termination, additional spurious growth attempts create short, small-diameter CNTs,[18,29] as seen for $t_{\mathrm{p}} \geq 40$ mins in Fig. S4. These short CNTs are not incorporated into the n scaling because they remain on the substrate after CNT array pull-off, *i.e.* are not removed in tensile testing, as they do not become entangled with the CNT array and therefore do not experience the tensile loading condition.[15] However, it is plausible that if these short CNTs physically contact the existing CNTs, they could contribute (although likely minimally) to local stresses during array pull-off. Studying these potential extra interactions *via* modeling and simulation at the CNT-substrate interface could be a future area of research to further elucidate the adhesion response mechanisms.

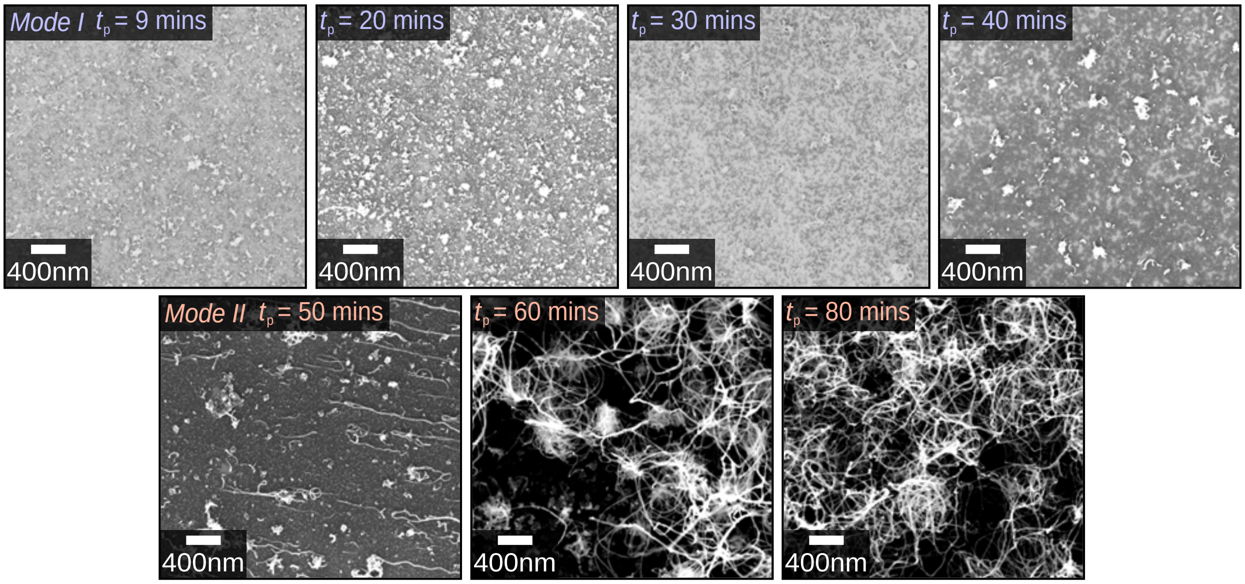

Fig. S4 SEM images showing the morphology of the Si wafer surface after CNT-substrate separation as t_p increases from 9 to 80 minutes through Mode I (‘Growth’) and Mode II (‘Post-Growth’). No catalyst pits are seen, and residual carbon on top of the Fe catalyst layer on the Si wafer substrates post-separation indicates that the weakest/separating interface for all t_p is between the crystalline CNT base and the carbon layer covering the Fe catalyst. At long process times, short ($\ll$ micron-long) CNTs remain on the wafer surface, as they are too short to experience the tensile loading condition and therefore are not removed from the substrate.

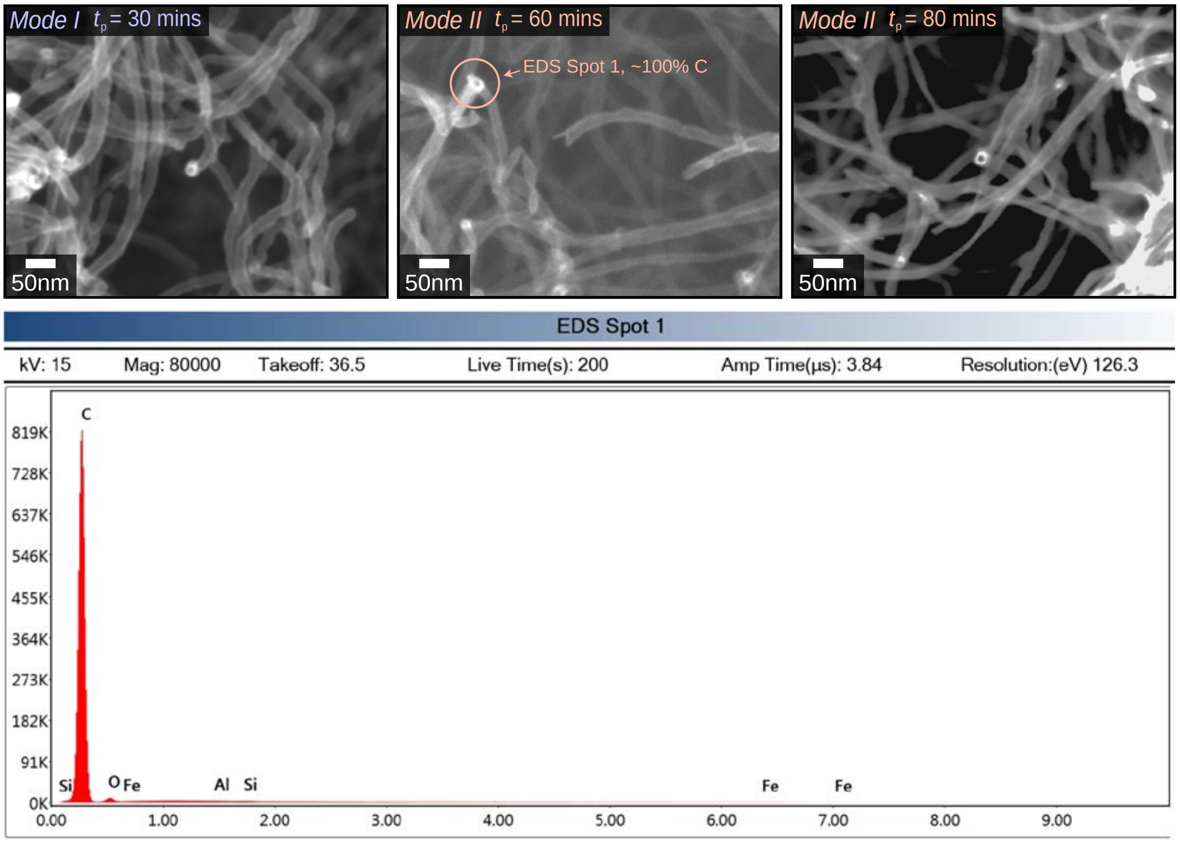

Fig. S5 SEM images showing the morphology of the CNT roots (*i.e.* CNT array surface that is separated from the substrate) after CNT-substrate separation at exemplary t_p values of 30 mins (Mode I, 'Growth') and 60 and 80 mins (Mode II, 'Post-Growth'). The open-ended, carbon-coated CNT roots are visible at each t_p and do not contain iron as confirmed by EDS (representative plot is shown here for a CNT root located at the base of the separated array for t_p = 60 min, with only carbon and oxygen species characteristic of CNTs). This result is observed for all tested t_p and shows that the iron catalyst particles are not attached to the CNT roots during CNT array pull-off, but instead remain on the substrate after tensile testing in each Mode. This further illustrates that the breaking interface in CNT array-substrate separation for this system is between the crystalline CNT base and the carbon layer covering the catalyst as a result of the growth process.

S3 CNT Array Structure and Morphology as a Function of CNT Process Time

To study the effect of t_p on $\sigma_\mathrm{a-s}$ evolution, the multiscale structure of CNT arrays synthesized for t_p up to 80 min was analyzed to provide a morphological framework to support the adhesion model. SEM and TEM were used to characterize the micro- and nano-scale CNT array morphology and CNT wall structure, respectively.[34] SEM analysis (see Fig. S6) was used to qualitatively determine the CNT array packing, waviness, and increases in wall thickness (a) and thereby the outer CNT radius due to carbon deposition on the CNT walls at increasing values of t_p in the Mode II post-growth regime. SEM was performed using a Zeiss Merlin High-resolution SEM with an accelerating voltage of 1 kV, 5 mm working distance, and the InLens detector. TEM analysis (see Fig. S7) was performed to measure a following Ref. 34, and to observe the number of CNT walls, outer CNT diameter, inner CNT diameter, and structural carbon character, including the accumulated carbon layers on the outer CNT walls as a function of t_p. TEM samples were prepared *via* the ultrasonication of CNT array sections in isopropyl alcohol for five mins. These CNTs were then dropcast onto a copper TEM grid, and the solvent was evaporated. The sample preparation of the TEM specimens was not limited to a specific location in the CNT array, and so the measured a values represent an average throughout the array for each t_p.[34] The TEM analysis was performed using a JEOL 2100 TEM at an accelerating voltage of 200 kV, and these results were used to support the adhesion model by experimentally quantifying the CNT wall structure and corresponding a evolution for t_p values up to 80 min.

After CNT growth was initiated in the CVD process, which synthesizes multiwalled mm-tall vertically aligned CNT arrays *via* base growth on flat wafer substrates composed of Fe/Al_2O_3/SiO_2/Si layers (see Methods in the main text), CNT growth was observed to progress through two distinct modes as a function of t_p (see Fig. S6). As discussed in the main text, Mode I represents steady vertical growth until growth termination,[17] at which point no further increase in CNT height (h) is observed (as measured *via* optical microscopy), although some spurious short CNT growth is observed as noted in Fig. S4 and related discussion. Mode II represents the post-growth regime of carbon deposition (*i.e.* disordered and rotationally faulted graphene-like layers), where additional carbon is deposited on the CNT walls due to prolonged exposure to carbon feedstock gas at the growth temperature (see Fig. 1 and Fig. 4 in the main text and Fig. S7).

The evolution of CNT array morphology with t_p, including h and a, is shown in Fig. S6 to detail the CNT structural evolution throughout the two Modes. As t_p increases, h increases *via* steady growth in Mode I and terminates at $t_\mathrm{p} \sim 40$ min, marked by a plateau in h throughout Mode II. The CNT growth profile can be quantified most simply by a bilinear fit, where Mode I is described as $h(t_\mathrm{p}) \propto \alpha_b t_\mathrm{p}$ with $\alpha_b \approx 0.11$ mm/min, signifying a CNT growth rate of ~ 0.11mm/min, consistent with prior literature for these systems.[36] At $t_\mathrm{p} \sim 40$ min, the system transitions to Mode II with constant $h \sim 4.68$ mm. An autocatalytic model more accurately quantifies CNT array growth by capturing the nonlinearity of the termination process and reaction kinetics, and this system can therefore be described by an autocatalytic fit *via* eqn S11:

$$h(t_\mathrm{p}) \propto \frac{\alpha_a}{1 + \mathrm{e}^{\kappa(t_\mathrm{p} - \tau)}} \tag{S11}$$

where α_a signifies the asymptotic final cumulative height of growth (~ 4.68 mm), κ is the reaction rate (~ 0.114 mm/min), and τ is the time origin (~ 21.1 min).[18] In both modes, a is observed to increase with t_p (see Fig. S6c). TEM analysis in Fig. S7 also shows that a increases with t_p, which is due to disordered carbon layers depositing on the CNT walls throughout the CVD synthesis. The increase of a with t_p is consistent with prior observations of pyrolytic and/or turbostratic carbon deposition on CNT walls and roots, especially at long t_p, as the growth conditions can facilitate carbon templating on CNTs with constant inner diameter after h stops increasing. In this way, carbon deposition on the outer CNT walls increases the CNT diameter, stiffens the array, and decreases the overall sp^2 carbon character both during growth[35,37,38] and during post-growth.[39–42] Here, the a evolution is described by a quadratic fit of the form $a \propto \chi(t_\mathrm{p})^2 + \varepsilon(t_\mathrm{p}) + \eta$, where $\chi \approx 0.000639$, $\varepsilon \approx 0.0215$, and $\eta \approx 1.08$. A quadratic scaling of a with t_p is therefore proposed to describe the increases in both a and the number of new CNT walls due to carbon deposition and templating, which becomes more dominant after growth termination and results in the thickest walls at the longest t_p.

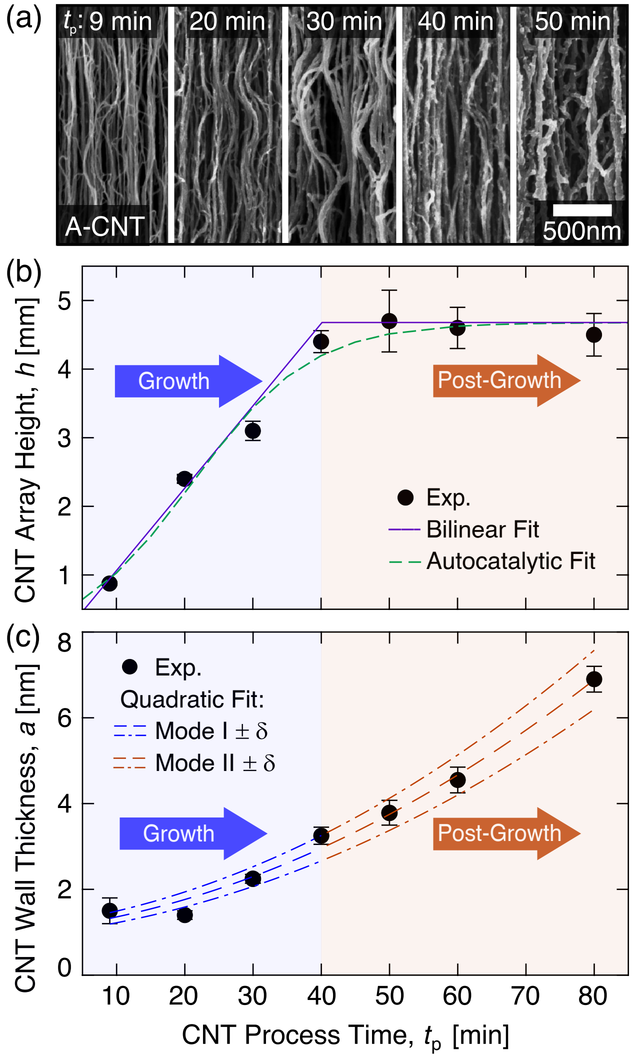

Fig. S6 Morphological evolution of vertically aligned CNT (A-CNT) arrays as a function of process time (t_p). (a) Scanning electron microscopy (SEM) images of the middle of the multiwalled A-CNT arrays showing the morphology evolution and qualitatively increasing CNT wall thickness (a) and therefore the outer CNT radius as t_p increases. (b) Plot showing how CNT height (h) evolves as a function of t_p in two distinct modes, which are separated by CNT growth termination occurring abruptly at $t_\mathrm{p} \sim 40$ min. A bilinear fit denotes the transition between Mode I (steady growth to growth termination) and Mode II (growth termination to carbon deposition, *i.e.* post-growth), and an autocatalytic fit describes the continuous h scaling with t_p.[18] (c) Plot and quadratic fit showing the scaling of a with t_p throughout Mode I and Mode II as measured *via* transmission electron microscopy, where δ represents standard error.

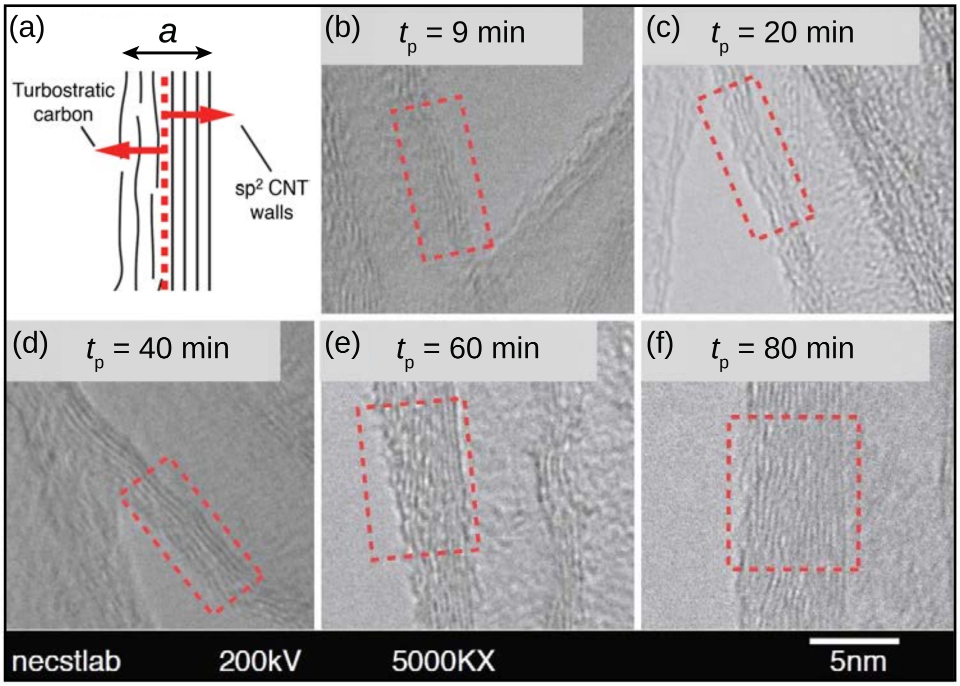

Fig. S7 Exemplary illustration (a) and representative TEM micrographs (b)-(f) of CNTs after CNT array-substrate separation, showing an increase in both the total CNT wall thickness (*a*) and the number of disordered carbon layers surrounding the CNT walls as the process time (t_p) increases from (b) 9 mins to (f) 80 mins, with the inner diameter remaining constant at ∼6 nm. When the CNTs remain at the growth temperature for longer t_p, carbon deposits on the outer CNT walls and uses the walls as a template to form slightly ordered carbon layers surrounding the CNTs. These layers appear more ordered closest to the original ∼ 3–6 CNT walls due to the templating effect and become more disordered towards the outer CNT diameter.

S4 Structural CNT Evolution *via* Raman Spectroscopy

To quantify the atomic-scale structural changes and bonding character evolution in the CNTs as a function of t_p, Raman spectroscopy was performed on the bottom of the CNT arrays after their separation from the wafer (*i.e.* by directing the Raman laser at the CNT roots/base where the array was previously attached to the substrate, see Fig. S3b).[43] This is done to assess the carbon crystallinity, relative defect densities, the effects of carbon accumulation in the CNT array based on processing conditions, and to provide potential explanations for changes in the surface energies of the CNT-substrate interfaces based on carbon character evolution.[44] Raman spectra were collected using a LabRam HR800 Raman microscope (Horiba Jobin Yvon) with 532 nm (2.33 eV) laser excitation through a 50× objective. Several spots on each CNT array sample (for at least 3 samples at each t_p) were studied so that representative data were used when calculating the intensity and areas of the Raman D- and G-bands. The D-band is found at a Raman shift (φ) of $\sim 1335-1350$ cm^{-1} for carbon materials and represents defects and disorder in the (002) plane, and the G-band is found at $\varphi \sim 1580-1600$ cm^{-1} and represents in-plane sp^2 bond stretching.[45] The intensity ($I_\mathrm{D}/I_\mathrm{G}$) and area ($A_\mathrm{D}/A_\mathrm{G}$) ratios of the D- and G-bands, as well as the half width at half maximum (H) of each band (H_D and H_G) were compared as a function of t_p, as these metrics are commonly used to determine the defect density and relative graphitization of carbon materials, such as aligned CNTs.

To analyze the native wall defects and bonding character of the CNT arrays, the Raman spectra were fit using two Lorentzian distributions corresponding to the graphitic D-band (centered at $\varphi_\mathrm{D} \sim 1350$ cm^{-1}) and amorphous carbon (a-C) G-band (centered at $\varphi_{\mathrm{G,a-C}} \sim 1500$ cm^{-1}), as well as the Breit-Wigner-Fano (BWF) distribution that corresponds to the graphitic G-band (centered at $\varphi_\mathrm{G} \sim 1590$ cm^{-1}). The fitting expressions detailed below yielded close agreement (coefficients of determination $\mathbb{R}^2 > 0.98$) with the experimental Raman spectra at 1000 cm^{-1} $\leq \varphi \leq$ 1800 cm^{-1}. $I_\mathrm{D}/I_\mathrm{G}$ was evaluated by using the I_D and I_G ratio from the Lorentzian and BWF fits of the D- and G-bands, while $A_\mathrm{D}/A_\mathrm{G}$ was evaluated by using the areas of the Lorentzian and BWF fits of the D- and G-bands (A_D and A_G, respectively). Background corrected Raman spectra, as characterized by φ and $I(\varphi)$, were fit using eqn S12 for the integration regions of the Raman D- and G-bands:[46]

$$I(\varphi) = I_\mathrm{D}\left(\frac{H_\mathrm{D}^2}{(\varphi-\varphi_\mathrm{D})^2+H_\mathrm{D}^2}\right) + I_{\mathrm{G,a-C}}\left(\frac{H_{\mathrm{G,a-C}}^2}{(\varphi-1500)^2+H_{\mathrm{G,a-C}}^2}\right) + I_\mathrm{G}\left(\frac{\left(1+\frac{\varphi-\varphi_\mathrm{G}}{qH_\mathrm{G}}\right)^2}{1+\left(\frac{\varphi-\varphi_\mathrm{G}}{H_\mathrm{G}}\right)^2}\right) \tag{S12}$$

where I_D and $I_{\mathrm{G,a-C}}$ are the Raman intensities of the Lorentzian distributions that fit the graphitic D-band and a-C G-band, respectively, and I_G and q are the Raman intensity and coupling coefficient of the BWF band that fits the graphitic G-band. Finally, A_D and A_G were evaluated as follows *via* eqn S13:

$$A_\mathrm{D} = \int_{\varphi_\mathrm{D}-\varphi_\mathrm{int}}^{\varphi_\mathrm{D}+\varphi_\mathrm{int}} I_\mathrm{D}\left(\frac{H_\mathrm{D}^2}{(\varphi-\varphi_\mathrm{D})^2+H_\mathrm{D}^2}\right)\mathrm{d}\varphi \tag{S13a}$$

$$A_\mathrm{G} = \int_{\varphi_\mathrm{G}-\varphi_\mathrm{int}}^{\varphi_\mathrm{G}+\varphi_\mathrm{int}} I_\mathrm{G}\left(\frac{\left(1+\frac{\varphi-\varphi_\mathrm{G}}{qH_\mathrm{G}}\right)^2}{1+\left(\frac{\varphi-\varphi_\mathrm{G}}{H_\mathrm{G}}\right)^2}\right)\mathrm{d}\varphi \tag{S13b}$$

where φ_int = 125 cm^{-1} corresponds to half the width of the Raman shift integration region centered around φ_D and φ_G.[46]

Fig. S8 shows representative Raman spectra and plots of the analysis results detailing the evolution of the I_D/I_G and A_D/A_G ratios, H_D, and H_G for the bottom of CNT arrays as a function of t_p. Large increases in both of these ratios at $t_p > 40$ min illustrate that the CNT defect density increases significantly due to additional carbon depositing on the outer CNT walls in Mode II, following growth termination. The plateau of I_D/I_G at $t_p > 50$ min shows that the most resonant Raman processes at longer t_p are better represented by a different set of modes/vibrations than those of the CNTs at earlier process times, which is attributed to the carbon character becoming more disordered in Mode II.[39,46] This is consistent with a non-sp^2 form of carbon in Mode II, such as rotationally faulted carbon layers covering the outer CNT walls. These CNT walls are originally more graphene-like in Mode I and exhibit a higher sp^2 character, as noted by the lower I_D/I_G and A_D/A_G ratios, consistent with the lower work of adhesion calculated by the fiber-substrate adhesion model in Mode I as described in the main text. In contrast, steady increases in A_D/A_G, H_D, and H_G at $t_p > 40$ min in Mode II ('Post-Growth') signify that there is a higher probability of CNT wall defects as t_p increases due to the accumulation of carbon on the outer CNT walls, consistent with the increased work of adhesion calculated for the separating CNT-substrate interfaces in Mode II.

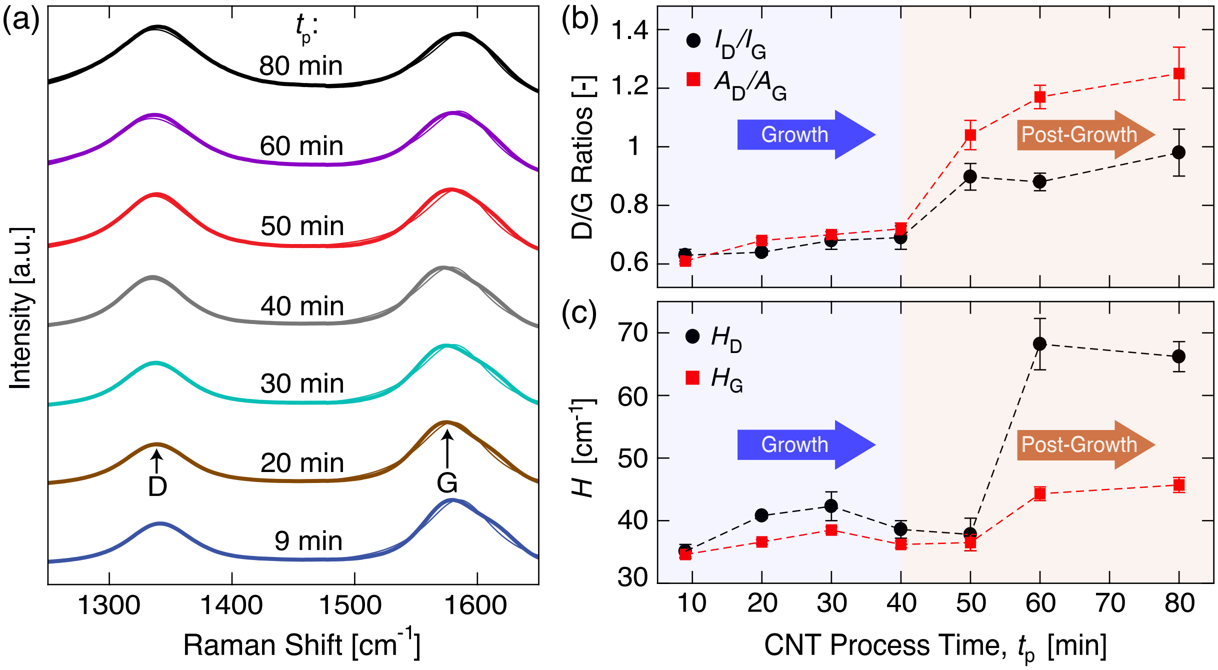

Fig. S8 Structural evolution of aligned CNT arrays as a function of CNT process time (t_p) characterized by Raman spectra taken at the base/underside of the CNT array after separation from the substrate. (a) Raman spectra of CNT arrays grown for t_p ranging from 9 to 80 min. The D- and G-peaks broaden as t_p increases, signifying that a higher percentage of defective, non-sp^2 carbon is present at longer process times. (b) Plot showing the evolution of the intensity (I_D/I_G) and area (A_D/A_G) ratios of the D- and G-bands with t_p. The higher ratios observed after growth termination at $t_p \sim 40$ min show that the overall CNT array defect density increases as carbon is deposited on outer CNT walls in Mode II ('Post-Growth'). (c) Plot showing the evolution of the half width at half maximum (H) of the D- and G-bands with t_p. The increasing H from Mode I ('Growth') to Mode II signifies the deposition of more defective carbon in the CNT array at long t_p.

The increased H also illustrates the deposition of more defective carbon in the CNT array at long t_p in Mode II. At these longer process times, $H_\mathrm{D} > H_\mathrm{G}$, because the CNT defect density (related to the D-band) increases with the accumulation of carbon, while the in-plane sp^2 bond stretching of the CNTs (related to the G-band) is less affected by increases in t_p.[39] This phenomenon is consistent with stage 2 in the three-stage amorphization trajectory presented in Ref. 44 and applied to defective graphene and pyrolytic carbon, where sp^3 character and defects are progressively introduced into stacked graphene layers. Matching closely with the Mode II values reported here, Ref. 47 reports $H_\mathrm{G} \sim 40\,\mathrm{cm}^{-1}$ for defective graphene in stage 2. Therefore, the carbon deposited at long t_p values is likely a fine-grained turbostratic (but not fully amorphous) form of carbon that templates on the outer CNT walls, creating carbon layers that have a lower crystallinity than the inherent CNT walls and giving rise to larger a (and presumed greater cumulative VDW interactions and surface energy/work of adhesion) at extended process times.[17]

References

[1] V. L. Popov, R. Pohrt, and Q. Li, Friction **5**, 308 (2017).

[2] V. Popov, M. Heß, and E. Willert, *Handbook of Contact Mechanics: Exact Solutions of Axisymmetric Contact Problems* (Springer Berlin Heidelberg, 2019).

[3] D. Tabor, J. Colloid Interface Sci. **58**, 2 (1977), international Conference on Colloids and Surfaces.

[4] K. Kendall, J. Phys. D: Appl. Phys. **4**, 1186 (1971).

[5] R. Spolenak, G. Stanislav, G. Huajian, and A. Eduard, Proc. Math. Phys. Eng. Sci. **461**, 305 (2005).

[6] S. Cranford, H. Yao, C. Ortiz, and M. J. Buehler, J. Mech. Phys. Solids **58**, 409 (2010).

[7] M. R. Maschmann, Carbon **86**, 26 (2015).

[8] Y. Won, Y. Gao, M. A. Panzer, R. Xiang, S. Maruyama, T. W. Kenny, W. Cai, and K. E. Goodson, Proc. Natl. Acad. Sci. U.S.A. **110**, 20426 (2013).

[9] I. Y. Stein, D. J. Lewis, and B. L. Wardle, Nanoscale **7**, 19426 (2015).

[10] H. Cebeci, I. Y. Stein, and B. L. Wardle, Appl. Phys. Lett. **104**, 023117 (2014).

[11] H. Gao, X. Wang, H. Yao, S. Gorb, and E. Arzt, Mech. Mater. **37**, 275 (2005), new Directions in Mechanics and Selected Articles in Micromechanics of Materials.

[12] P. Pour Shahid Saeed Abadi, S. B. Hutchens, J. R. Greer, B. A. Cola, and S. Graham, Appl. Phys. Lett. **102**, 223103 (2013).

[13] M. R. Roenbeck, X. Wei, A. M. Beese, M. Naraghi, A. Furmanchuk, J. T. Paci, G. C. Schatz, and H. D. Espinosa, ACS Nano **8**, 124 (2014).

[14] V. Tinnemann, L. Hernandez, S. C. L. Fischer, E. Arzt, R. Bennewitz, and R. Hensel, Adv. Funct. Mater. **29**, 1807713 (2019).

[15] J. Brown, T. Hajilounezhad, N. T. Dee, S. Kim, A. J. Hart, and M. R. Maschmann, ACS Appl. Mater. Interfaces (2019), 10.1021/acsami.9b09979.

[16] Y. Chen, D. Ding, C. Zhu, J. Zhao, and T. Rabczuk, Composite Structures **208**, 150 (2019).

[17] M. Bedewy, E. R. Meshot, and A. J. Hart, Carbon **50**, 5106 (2012).

[18] M. Bedewy, E. R. Meshot, M. J. Reinker, and A. J. Hart, ACS Nano **5**, 8974 (2011).

[19] I. Y. Stein and B. L. Wardle, Phys. Chem. Chem. Phys. **18**, 694 (2016).

[20] M. R. Roenbeck, A. Furmanchuk, Z. An, J. T. Paci, X. Wei, S. T. Nguyen, G. C. Schatz, and H. D. Espinosa, Nano Lett. **15**, 4504 (2015).

[21] M. Xia, C. Liang, Z. Cheng, R. Hu, and S. Liu, Phys. Chem. Chem. Phys. **21**, 1217 (2019).

[22] C. L. Pint, Y.-Q. Xu, M. Pasquali, and R. H. Hauge, ACS Nano **2**, 1871 (2008).

[23] M. De Volder, S. H. Tawfick, S. J. Park, D. Copic, Z. Zhao, W. Lu, and A. J. Hart, Adv. Mater. **22**, 4384 (2010).

[24] M. Bedewy, J. Mater. Res. **32**, 153–165 (2017).

[25] M. Stadermann, S. P. Sherlock, J.-B. In, F. Fornasiero, H. G. Park, A. B. Artyukhin, Y. Wang, J. J. De Yoreo, C. P. Grigoropoulos, O. Bakajin, A. A. Chernov, and A. Noy, Nano Lett. **9**, 738 (2009).

[26] V. Balakrishnan, M. Bedewy, E. R. Meshot, S. W. Pattinson, E. S. Polsen, F. Laye, D. N. Zakharov, E. A. Stach, and A. J. Hart, ACS Nano **10**, 11496 (2016).

[27] S. Jeong, J. Lee, H.-C. Kim, J. Y. Hwang, B.-C. Ku, D. N. Zakharov, B. Maruyama, E. A. Stach, and S. M. Kim, Nanoscale **8**, 2055 (2016).

[28] J. Lee, I. Y. Stein, M. E. Devoe, D. J. Lewis, N. Lachman, S. S. Kessler, S. T. Buschhorn, and B. L. Wardle, Appl. Phys. Lett. **106**, 053110 (2015).

[29] M. Bedewy, E. R. Meshot, H. Guo, E. A. Verploegen, W. Lu, and A. J. Hart, J. Phys. Chem. C **113**, 20576 (2009).

[30] Y. Gao, T. Kodama, Y. Won, S. Dogbe, L. Pan, and K. E. Goodson, Carbon **50**, 3789 (2012).

[31] J.-P. Salvetat, J.-M. Bonard, N. H. Thomson, A. J. Kulik, L. Forro, W. Benoit, and L. Zuppiroli, Appl. Phys. A **69**, 255 (1999).

[32] W. Li, Y. Li, M. Sheng, S. Cui, Z. Wang, X. Zhang, C. Yang, Z. Yu, Y. Zhang, S. Tian, Z. Dai, and Q. Xu, Langmuir **35**, 4527 (2019).

[33] I. Lahiri, D. Lahiri, S. Jin, A. Agarwal, and W. Choi, ACS Nano **5**, 780 (2011).

[34] D. L. Lidston, *Synthesis, characterization, and mode I fracture toughness of aligned carbon nanotube polymer matrix nanocomposites*, Master's thesis, Massachusetts Institute of Technology (2017).

[35] X. Cui, W. Wei, C. Harrower, and W. Chen, Carbon **47**, 3441 (2009).

[36] E. S. Avraham, A. S. Westover, A. Itzhak, L. Shani, V. Mor, O. Girshevitz, C. L. Pint, and G. D. Nessim, Carbon **130**, 273 (2018).

[37] X. Li, X. Zhang, L. Ci, R. Shah, C. Wolfe, S. Kar, S. Talapatra, and P. M. Ajayan, Nanotechnology **19**, 455609 (2008).

[38] S. Yasuda, T. Hiraoka, D. N. Futaba, T. Yamada, M. Yumura, and K. Hata, Nano Lett. **9**, 769 (2009).

[39] S. Santangelo, M. Lanza, and C. Milone, J. Phys. Chem. C **117**, 4815 (2013).

[40] V. Thiagarajan, X. Wang, P. Bradford, Y. Zhu, and F. Yuan, Compos. Sci. Technol. **90**, 82 (2014).

[41] A. A. Puretzky, D. B. Geohegan, S. Jesse, I. N. Ivanov, and G. Eres, Appl. Phys. A **81**, 223 (2005).

[42] C. Singh, M. S. Shaffer, and A. H. Windle, Carbon **41**, 359 (2003).

[43] A. L. Kaiser, *Capillary densification and adhesion tuning of aligned carbon nanotube arrays for shape-engineerable architectures*, Master's thesis, Massachusetts Institute of Technology (2019).

[44] A. C. Ferrari and J. Robertson, Phys. Rev. B **61**, 14095 (2000).

[45] M. S. Dresselhaus, A. Jorio, M. Hofmann, G. Dresselhaus, and R. Saito, Nano Lett. **10**, 751 (2010).

[46] I. Y. Stein, A. L. Kaiser, A. J. Constable, L. Acauan, and B. L. Wardle, J. Mater. Sci. **52**, 13799 (2017).

[47] L. G. Cancado, A. Jorio, E. H. M. Ferreira, F. Stavale, C. A. Achete, R. B. Capaz, M. V. O. Moutinho, A. Lombardo, T. S. Kulmala, and A. C. Ferrari, Nano Lett. **11**, 3190 (2011).